Rheological measurements on dense suspensions containing dendrite-like particles

Andreas Ludwig, Mihaela Stefan-Kharicha, Christian Gomes Rodrigues, Johann Mogeritsch, Menghuai Wu, and Abdellah Kharicha

Technical University Leoben, Department Metallurgy, Franz-Josef Strasse 18, 8200 Leoben, Austria

(Received 13 February 2026; accepted 12 June 2026; published 22 July 2026)

During alloy solidification, equiaxed dendrites often move within the solidifying liquid. As this motion is one of the main causes of macrosegregation, a deeper understanding of the behavior of suspensions containing dendrite-like particles is particularly important. Inspired by rheological investigations with dense suspensions containing spheres, pressure-imposed rheological measurements using an annular shear cell were performed and applied to suspensions containing 3D-printed dendrite-like particles. The results indicate that the concept of the friction coefficient for spheres can be adapted by using appropriate coefficients and suitably reduced mechanical coherency limits. Consequently, the particle pressure of interacting, moving dendrite-like particles in liquids can be effectively described. However, direct measurement of the shear rate was not possible due to the shallowness of the rheological cell used. Nevertheless, the viscosity of suspension containing dendrite-like particles could be estimated indirectly by adapting the dimensionless friction number originally proposed for suspensions with spheres. An increase in viscosity at the same reduced solid fraction, due to the specific morphology of the dendrite-like particles, is predicted. While spheres predominantly interact by sliding past one another, dendrite-like particles—particularly those with long sidearms—interact mainly through rotation.

DOI: 10.1103/nmkb-mj7x

I. INTRODUCTION

As alloys solidify, equiaxed crystals often occupy large regions within a casting [1,2]. Therefore, an exact prediction of the microstructure is only possible when the formation, growth, and transport of these crystals are thoroughly understood [3–5]. However, one aspect that remains poorly understood is the transport of equiaxed crystals, especially as influenced by buoyancy or forced convection. While studies involving single crystals [6–9] or loosely packed assemblages [10] provide useful data, they are insufficient when the crystal-crystal interactions become significant. For this reason, Beckermann *et al.*, in their pioneering work on solidification volume-averaging models [11,12], adopted the well-known Krieger–Dougherty expression [13,14] for the mixture viscosity of suspensions of rigid spheres, which varies with solid fraction, g_s, as

$$\eta_{\mathrm{mix}} = \eta_\ell \left(1 - \frac{g_s}{g_{s,c}}\right)^{-2.5 g_{s,c}}, \tag{1}$$

where $g_{s,c}$ is a critical volume fraction at which η_{mix} tends to infinity and the crystal-melt mixture ceases to flow. Here, η_ℓ in Eq. (1) represents the viscosity of the melt without any crystals. The authors stated that this approach accounts for the presence of multiple crystals and their interactions within the averaging volume.

The expression in Eq. (1) was also extensively used to predict the microstructure of large castings, specifically accounting for the sedimentation of equiaxed crystals [15–17]. The key limitation in these studies was the assumption of globular equiaxed crystals and the use of the random close packing limit of equally sized spheres for $g_{s,c}$. Subsequent developments of the solidification volume-averaging model addressed the fact that, in most cases, equiaxed crystals exhibit a dendritic shape rather than being spherical. This was accounted for by differentiating between extra- and interdendritic melt [18,19]. The commonly used model of this kind considers an octahedral equivalent envelope shape to separate the extra- and interdendritic melt. It also introduced the concept of sphericity for the effective surface area through which diffusion occurs from the dendritic grains into the bulk melt [20,21]. However, Eq. (1) was continued to be applied, with g_s now representing the volume fraction of the sum of both the dendritic solid and the interdendritic liquid. It is important to note that the interdendritic melt was assumed to move in conjunction with the dendritic crystals. Sphericity,Ψ, is the ratio of the surface area of an equivalent sphere to the surface area of a non-spherical particle with the same volume as the equivalent sphere.

Within the solidification community, the jamming point at $g_{s,c}$ is referred to as the mechanical coherency or rigidity point, and it should be distinguished from the dendritic coherency point. As outlined by Dahle and St. John [22], the behavior of a semisolid mush (a term used by the solidification community for the corresponding suspension) can be divided into three regions of distinct mechanical and feeding behaviors. For g_s below the dendritic coherency point, the semisolid mush (dendritic suspension) exhibits no measurable shear strength, as interactions between individual crystals can be neglected. Between the dendritic and the mechanical coherency points, crystal-crystal interactions cause the shear strength to

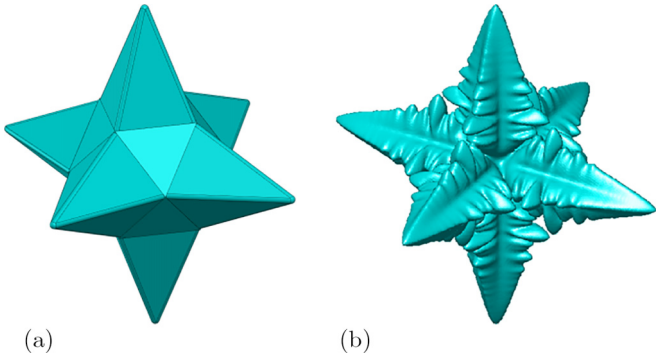

FIG. 1. (a) Rendered image of an OSP6 (six quadrilateral pyramids attached to the six square faces of a cuboctahedron), and (b) fcc 'phase field' crystal similar to that shown in Fig. 2 of [26], provided by one of the authors (M.R.). The OSP6 approximation captures the overall geometry of a sixfold dendritic equiaxed crystal, excluding the details of the secondary sidearms.

increase. When g_s exceeds the mechanical coherency point, solid bridges form between the crystals, enabling the transmission of stresses through the solid skeleton [23]. However, due to the high shear stresses involved in the third regime, it is not relevant for the present study.

It is well known that both the dendritic and the mechanical coherency points are strongly influenced by the morphology of the crystals [22,24]. Alloys that solidify with dendritic grains have significantly lower transition points compared to alloys that solidify more globularly. Olmedilla *et al.* [10] compared the sedimentation behavior of spherical particles with that of hexapod particles (which have a sphericity of less than one). They found the packing fraction for hexapods in glycerol is $g_{s,c} \approx 0.4$, compared to $g_{s,c} \approx 0.6$ for spheres. The volume-averaged packing fraction in the packed bed was calculated as the ratio of the total volume of the particles to the total volume occupied by the packed bed. This quantity corresponds to the critical solid fraction at the jamming point, assuming random, very loose packing. Alongside their experimental work, Olmedilla *et al.* performed discrete element method (DEM) simulations and suggested that the packing limit depends on the sphericity of their simplified equiaxed hexapods.

Approximating dendritic equiaxed crystals with six quadrilateral pyramids attached to a central cube, as suggested by Olmedilla *et al.* [10], is relatively uncommon. A more frequently used approximation is to attach the six quadrilateral pyramids to the six square faces of a cuboctahedron (abbreviated as OSP6). This shape was used by de Groh *et al.* in 1993 [6], by Badillo *et al.* in 2007 [8,9], and by the author's team in 2010 [25] within a volume-averaging solidification model. The rationale for using this approximation is that it closely envelopes the primary and secondary arm tips of an equiaxed dendritic crystal, which typically exhibits fcc or bcc crystallography. In Fig. 1, an OSP6 object is compared to a simulated fcc 'phase field' crystal that realistically reproduces the shape of equiaxed crystals [26]. While the OSP6 approximation neglects some details of the secondary sidearms, it effectively captures the main features of the crystal shape.

As outlined in [6], an OSP6 object is fully characterized by two parameters: (i) the pyramid angle, α, defined as the angle between the primary dendrite arm axis and a straight line connecting the tips of the secondary arms, and (ii) the distance between the tips of two opposing pyramids, d_{OSP6}. With these two parameters, the volume and the surface area of an OSP6 can be calculated. The sphericity of an OSP6 can be expressed solely as a function of α.

Boyer *et al.* [27] found that dense suspensions containing spherical particles of equal size can be fully characterized by the evolution of two quantities: the friction coefficient, $\mu = \tau/P^p$, and the dimensionless viscous number, $I_v = \eta_f \dot{\gamma}/P^p$. Using these two quantities, the shear stress, τ, and the particle pressure, P^p, can be expressed as functions of the shear rate, $\dot{\gamma}$, as follows:

$$\tau = \mu P^p = \eta_f \frac{\mu}{I_v}\dot{\gamma} = \eta_f \eta_s \dot{\gamma}, \tag{2}$$

and

$$P^p = \eta_f \frac{1}{I_v}\dot{\gamma} = \eta_f \eta_n \dot{\gamma}, \tag{3}$$

where η_f is the viscosity of the suspending liquid, $\eta_s = \mu/I_v$ is the dimensionless shear viscosity, and $\eta_n = 1/I_v$ is the dimensionless normal viscosity of the suspension. For μ and I_v, Boyer *et al.* [27] found the following relationships:

$$\mu(g_s) = \underbrace{\mu_1 + \frac{\mu_2 - \mu_1}{1 + I_0/\left(\frac{g_{s,c}-g_s}{g_s}\right)^2}}_{=\mu_c} + \underbrace{\left(\frac{g_{s,c}-g_s}{g_s}\right)^2 + \mu_3 g_{s,c}\left(\frac{g_{s,c}-g_s}{g_s}\right)}_{=\mu_h}, \tag{4}$$

and

$$I_v(g_s) = \left(\frac{g_{s,c} - g_s}{g_s}\right)^2. \tag{5}$$

As empirical quantities, they used $\mu_1 = 0.32$, $\mu_2 = 0.7$, $\mu_3 = 2.5$, and $I_0 = 0.005$. The quantity μ_c was identified as the contact friction coefficient and μ_h as the hydrodynamic contribution to the friction coefficient. The solid volume fraction at which the viscosity of the suspension diverges was found to be $g_{s,c} = 0.585$.

Boyer *et al.* [27] obtained their findings by conducting pressure-imposed rheological measurements using an annular shear cell. This setup confined a suspension of solid spheres in a Newtonian liquid between a static truncated cone and a rotating annulus. The annulus was semipermeable and free to move vertically. The input parameters for the experiments were the torque, M, and the force, F, exerted by the rotating annulus on the suspension. The measurements captured the resulting rotational speed, ω, and the vertical displacement of the annulus, δ, after reaching quasi-steady-state conditions, typically after around 30 minutes. Initially, the suspension had a solid volume fraction of g_{s0} with the annulus positioned at $\delta = 0$ with a zero normal force. From the measured M and F, the shear stress, $\tau = 3M/2\pi(R_2^3 - R_1^3) = \alpha_M M$, and the particle pressure, $P^p = F/\pi(R_2^2 - R_1^2) = \alpha_F F$, were calculated. Boyer *et al.* used $R_1 = 44$ mm and $R_2 = 90$ mm as the inner and the outer radii

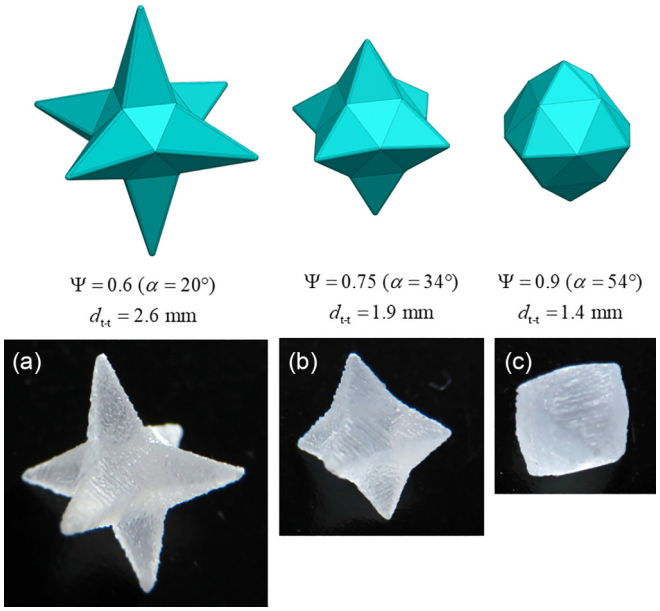

FIG. 2. CAD models and 3D-printed OSP6 particles with different sphericities, Ψ, and tip angles, α. Although particles A, B, and C differ markedly in their tip-to-tip length, they each encapsulate the same volume.

of the rheometer, and thus got $\alpha_M = 741.62\,\mathrm{m}^{-3}$ and $\alpha_F = 51.64\,\mathrm{m}^{-2}$. The resulting solid volume fraction could be calculated from the measured δ value as $g_s = g_{s0}/(1+\alpha_\delta\delta)$ with $\alpha_\delta = [3R_2(R_2^2-R_1^2)]/[2(R_2^3-R_1^3)H_2] = 71.81\,\mathrm{m}^{-1}$. This was derived from straightforward geometrical arguments, with $H_2 = 18$ mm being the cell depth at the outer radius R_2 when $\delta = 0$.

This report describes our attempt to replicate the experiment outlined by Boyer *et al.* [27], replacing the spherical particles by 3D-printed, dendrite-like OSP6 particles of comparable size. In addition, it investigates whether Eq. (1) remains a good approximation for the mixture viscosity of a suspension containing equal-sized OSP6 particles when the parameter $g_{s,c}$ is adjusted to account for particle sphericity.

II. EXPERIMENTAL PROCEDURE

A. 3D-printed dendrite-like OSP6 particles

In order to perform rheological measurements on suspensions containing OSP6 particles of equal size, a sufficient amount of particles was produced. We used OSP6 particles with sphericities of Ψ = 0.6, 0.75, and 0.9 (Fig. 2), corresponding to tip angles of $\alpha = 20°$, 34°, and 54°. According to Olmedilla *et al.* [10], objects with these sphericity values are expected to have packing limits of $g_s^c = 0.35$, 0.42, and 0.51 (taken from Fig. 6 in [10]). Assuming that all produced OSP6 particles had an equivalent sphere radius comparable to the larger spheres used by Boyer *et al.* ($r_{e,\mathrm{OSP6}} = 0.55$ mm), it was necessary to produce approximately 102 000 A-type particles with Ψ = 0.6, 122 000 B-type particles with Ψ = 0.75, and 149 000 C-type particles with Ψ = 0.9. These quantities were calculated to achieve maximum filling of the rheometer cell for different $g_{s,c}$. The corresponding tip-to-tip lengths were $d_{t-t} = 2.6$ mm, 1.9 mm, and 1.4 mm. Figure 2 shows CAD models and detailed views of the 3D-printed OSP6 particles, while Fig. 3 presents ensembles of the different OSP6 particle types.

The OSP6 particles were produced using a ProJet Multi Jet Printing 2500Plus 3D printer with VisiJet® Armor M2G-HT90 as the particle material, which has a density of $1.15\,\mathrm{g/cm}^3$. In this process, the liquid photopolymer resin is sprayed onto a build platform through fine nozzles in a print head. A UV light source then passes over the fine droplets and cures each layer. During printing, the objects are supported with paraffin, which is subsequently melted away during post-processing.

For paraffin removal, a constantly stirred water–particle suspension was maintained at 80 °C, while a filter-screen piston was slowly lowered, pressing the particles downward as the paraffin floated to the surface. This procedure separated the particles from the paraffin, causing the particles to sink in the water. Finally, the particles were collected using a sieve and then dried. Some of them were colored with ink for tracking purposes.

B. The rheological experiments

Pressure-imposed rheological measurements on dense suspensions were conducted using a self-constructed annular shear cell mounted on an Anton Paar MCR 702 rheometer, following a procedure similar to that described by Boyer *et al.* [27]. Three different sets of dendrite-like OSP6 particles (types A, B, and C), produced by 3D printing, were dispersed in glycerol or PEG-PPG.

For a given solid fraction of a specific particle type, and for fixed values of torque and normal force, the rotation rate and the cover position were recorded as functions of time. Typically, 10 to 12 measurements were performed sequentially, with each experiment lasting 1800 s. After this period, the torque and normal force were automatically adjusted. Figure 4 shows an example of such a set of measurements. All measurement data used in this publication are available under [28]. Further details and a schematic illustration of the experimental setup can be found in [27].

In their experiment, Boyer *et al.* used two systems: (i) poly(methyl methacrylate) (PMMA) spheres ($d = 1.10$ mm) in a Triton X-100/water/zinc chloride mixture with $\eta_f = 3.1$ Pa·s, and (ii) polystyrene (PS) spheres ($d = 0.58$ mm) in polyethylene glycol-ran-propylene glycol monobutyl ether (PEG-PPG) with $\eta_f = 2.15$ Pa·s at 25 °C. We could not use the Triton X-100 mixture because its use has been restricted in the European Union since 2021 due to endocrine-disrupting degradation products. We have thus used glycerol ($\eta_f = 1.48$ Pa·s at 20 °C) as an alternative. The density of glycerol is $\rho = 1.26\,\mathrm{g/cm}^3$ at 25 °C, and that of PEG-PPG $\rho = 1.05\,\mathrm{g/cm}^3$ at 20 °C. $\eta_f = aT^2 + bT + c$ with $a = 0.0048\,\mathrm{Pa\cdot s/°C^2}$, $b = -0.3177\,\mathrm{Pa\cdot s/°C}$, and $c = 5.8987$ Pa·s and $a = 0$, $b = -0.122\,\mathrm{Pa\cdot s/°C}$, and $c = 5.2$ Pa·s were assumed for the temperature dependence of the viscosity of glycerol and PEG-PPG, respectively.

Our replica of Boyer's rheometer cell had slightly different dimensions. We measured $R_1 = 43.7$ mm, $R_2 = 90.6$ mm, $H_1 = 8.6$ mm, and $H_2 = 17.56$ mm, which yielded values of $\alpha_M = 723.19\,\mathrm{m}^{-3}$, $\alpha_F = 50.54\,\mathrm{m}^{-2}$, and $\alpha_\delta = 73.58\,\mathrm{m}^{-1}$ for

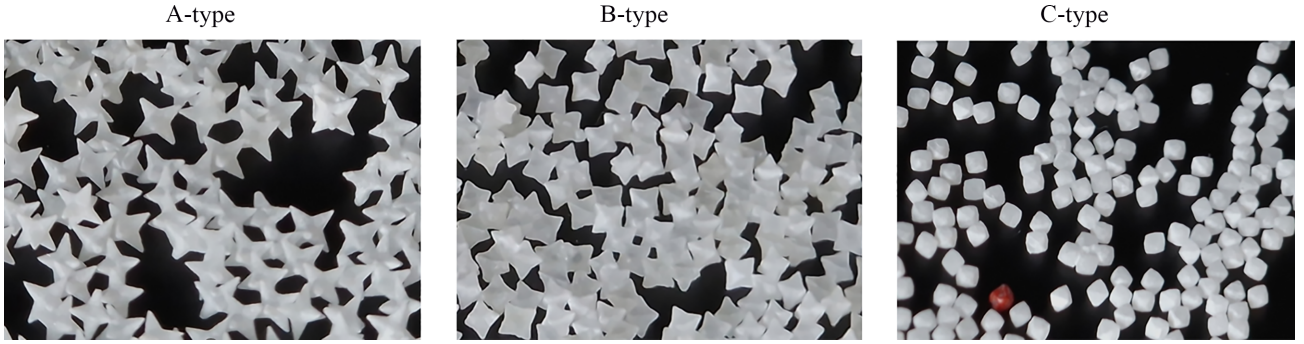

FIG. 3. Ensembles of 3D-printed dendrite-like particles that reproduce the envelope shape of equiaxed dendritic crystals commonly formed during alloy solidification. Some of the particles were colored to aid tracking during the rheological experiments.

the constants that relate the shear stress, τ, to the torque, M, the pressure, P^p, to the force, F, and the solid fraction, g_s, to the change in the cover position, $\delta = \Delta d$, respectively.

The rheometer was operated with two different porous covers (rotating annuli) with slightly different radii: $R_1 = 44.1$ mm and $R_2 = 89.9$ mm for the first cover, and $R_1 = 44.25$ mm and $R_2 = 89.75$ mm for the second. These dimensions resulted in inner and outer gaps of 0.4 mm and 0.7 mm for the first cover, and 0.55 mm and 0.85 mm for the second. For both covers, careful adjustment was required to ensure frictionless rotation at different vertical positions of the cover.

Interstitial fluid passed through the porous cover via 5 mm holes covered with a 200 μm nylon mesh. The lower surface of the covers was roughened by gluing steel bars onto them: 60 bars with a 0.5-mm-square cross section on the first cover, and 45 bars with a 1.5-mm-square cross section on the second. The first cover was used for experiments with B- and C-type particles, whereas the second cover was used for A-type particles. On the bottom side, 45 Plexiglas bars with a 1.5-mm-square cross section were mounted on the static truncated cone.

Figure 4 shows a typical sequence of twelve experimental measurements. The torque, M, and the normal force, F, were held constant at predefined inputs, while the resulting rotation speed, ω, and the vertical cover position, d, were recorded as responses. In order to compensate for the hydrostatic weight of the suspension column, F was set to zero before the start of the experimental run. For each measurement, the system was allowed to approach a quasi-steady-state condition over a duration of 1800 s. However, as demonstrated in Fig. 4, steady-state conditions for ω, d, or both were not always reached within the 1800 s window. The corresponding data from these specific intervals were therefore omitted from the subsequent analysis. For each valid measurement, the

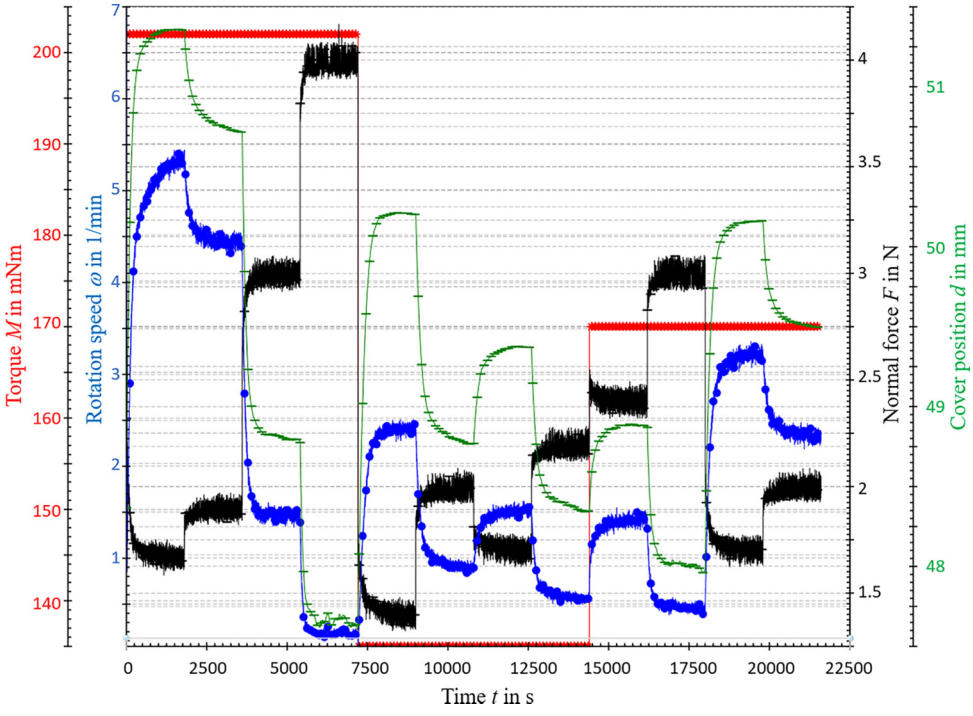

FIG. 4. Example of 12 measurements, each lasting 1800 s, for A-type particles in PEG-PPG. The process parameters included torques of $M = 202$, 135, and 170 mNm, and normal forces of $F = 1.67$, 1.9, 3.0, 4.0, 1.44, 2.0, 1.7, 2.2, 2.4, 3.0, 1.7, and 2.0 N. The rotation speed ω and the cover position d were recorded under quasi-steady-state conditions.

TABLE I. Applied coefficients for the friction coefficient of particles of A-, B-, and C-type in glycerol and PEG-PPG and corresponding values for spheres from Boyer *et al.* [27]. In all cases, $\mu_3 = 2.5$ was set. The data labeled with "Eq. μ_2/I_0" were used for the $\mu(g_s)$ functions on which the curves in Figs. 6–8 are based.

	A	B	C	Spheres [27]
$g_{s,c}$	0.310	0.395	0.465	0.585
μ_1	0.70	0.60	0.55	0.32
Eq. μ_2/I_0	2.25/0.123	3.50/0.313	2.50/0.080	0.7/0.005
Eq.+ μ_2/I_0	4.00/0.385	10.5/1.364	3.75/0.200	
Eq.- μ_2/I_0	1.75/0.050	2.10/1.03	2.00/0.034	

resulting values of M, F, ω and d were used to calculate the friction coefficient (μ) and the dimensionless viscous number (I_v), which are the quantities used to fully characterize the suspension.

III. RESULTS

Figure 5 shows the measured friction coefficient, $\mu = \tau/P^p$, as a function of solid volume fraction, g_s, for the three different dendrite-like particle types (A, B, and C) in both glycerol and PEG-PPG. As discussed in the next section, for Fig. 5, P^p (and thus μ) has not been modified to account for buoyancy effects.

When processing A-type particles, it occasionally occurred that a particle tip entered the gap between the rotation annulus and the cell wall. This had immediate observable consequences: either the measured force began to fluctuate irregularly, or the rotation stopped completely. We therefore evaluated only those measurements for the A-type particles in which no force irregularities occurred.

The solid and dashed lines, which approximately match the measurements, were estimated based on the following considerations.

(1) The solid volume fraction at which the viscosity of the suspension diverges, $g_{s,c}$, was assumed to be independent of the liquid medium. It was initially approximated using Fig. 6 of Ref. [10] and subsequently refined by simultaneously varying $g_{s,c}$ and μ_1 such that (i) an acceptable agreement between the $\mu - g_s$ curves and the measurements at larger g_s values and (ii) an acceptable agreement between the $\omega\eta_f - g_s$ curves and the corresponding measurements at larger g_s values (see below) were achieved. Note that the $\mu - g_s$ curves exhibit a minimum at $g_s = g_{s,c}$ and $\mu = \mu_1$. Using this procedure, an uncertainty of ± 0.005 for $g_{s,c}$ and ± 0.003 for μ_1 must be considered.

(2) The contact friction coefficient, $\mu_c = \mu_1 + (\mu_2 - \mu_1)/[1 + I_0((g_{s,c} - g_s)/g_s)^{-2}]$, [see Eq. (4)], was assumed to depend only on the particle type and not on the liquid type. The coefficients μ_2, and l_0 were varied to achieve an acceptable agreement between the $\mu - g_s$ curves for a given particle type and the measurements (in both liquids).

(3) The hydrodynamic friction coefficient, $\mu_h = ((g_{s,c} - g_s)/g_s)^2 + \mu_3 g_{s,c}((g_{s,c} - g_s)/g_s)$, [see Eq. (4)], was assumed to be identical for both liquids and equal to that of spheres with $\mu_3 = 2.5$, in accordance with Einstein's PhD thesis [29–31]. Consequently, in the limit of a vanishing solid fraction, Einstein's well-known expression for the mixture viscosity is recovered.

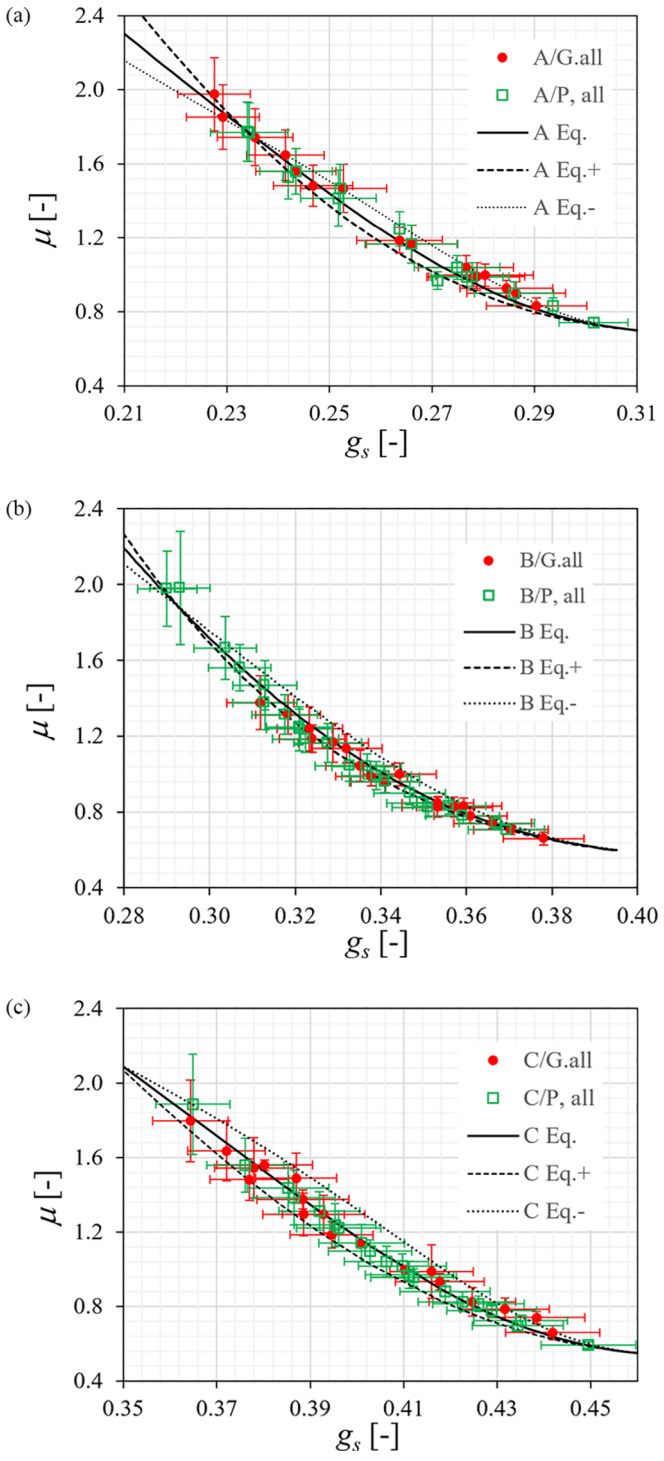

FIG. 5. Friction coefficient as a function of solid volume fraction for A, B, and C particles in glycerol (red) and PEG-PPG (green). The solid and dashed lines have been estimated according to the explanations given in the text.

Table I presents the estimated values of $g_{s,c}$, μ_1, μ_2, and l_0 that provide a good fit for the solid lines to the measured data. At large solid fractions, the $\mu - g_s$ curve is highly sensitive to the chosen values of $g_{s,c}$ and μ_1. However, the values of μ_2 and l_0 become imprecise. Smaller values of μ_2 and slightly

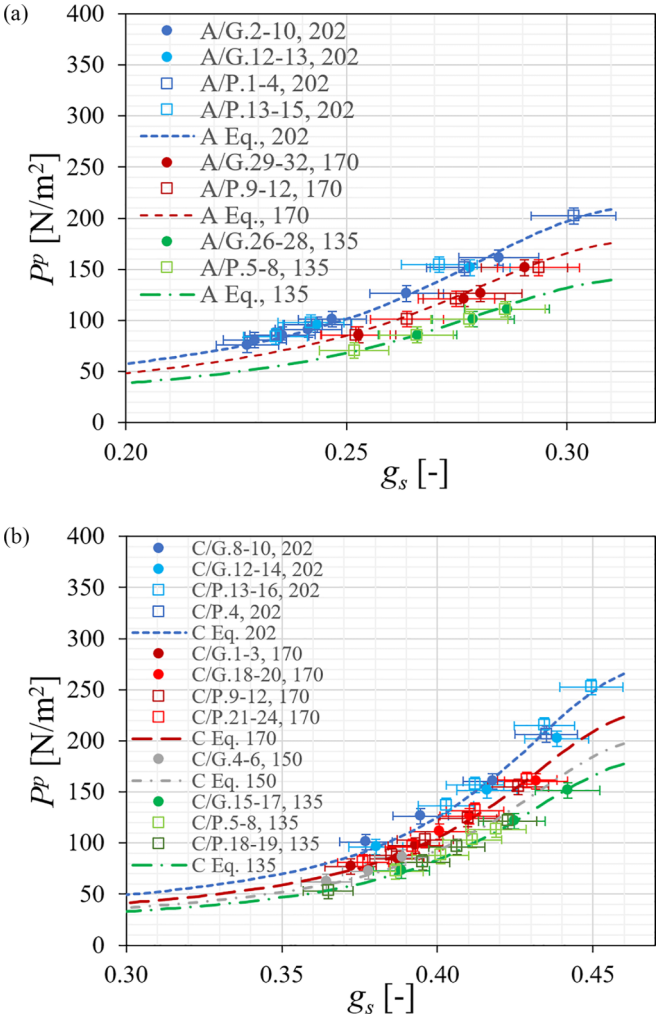

FIG. 6. Particle pressure as a function of solid volume fraction for A particles (a) and C particles (b) processed in both glycerol and PEG-PPG at different applied torques ($M = 135$, 150, 170, 202 mNm, as also indicated by the numbers given in the legend). The dashed lines correspond to the results from Eq. (6), based on the friction coefficient parameters established in Table I with μ_2 and l_0 taken from the Eq. μ_2/I_0 data.

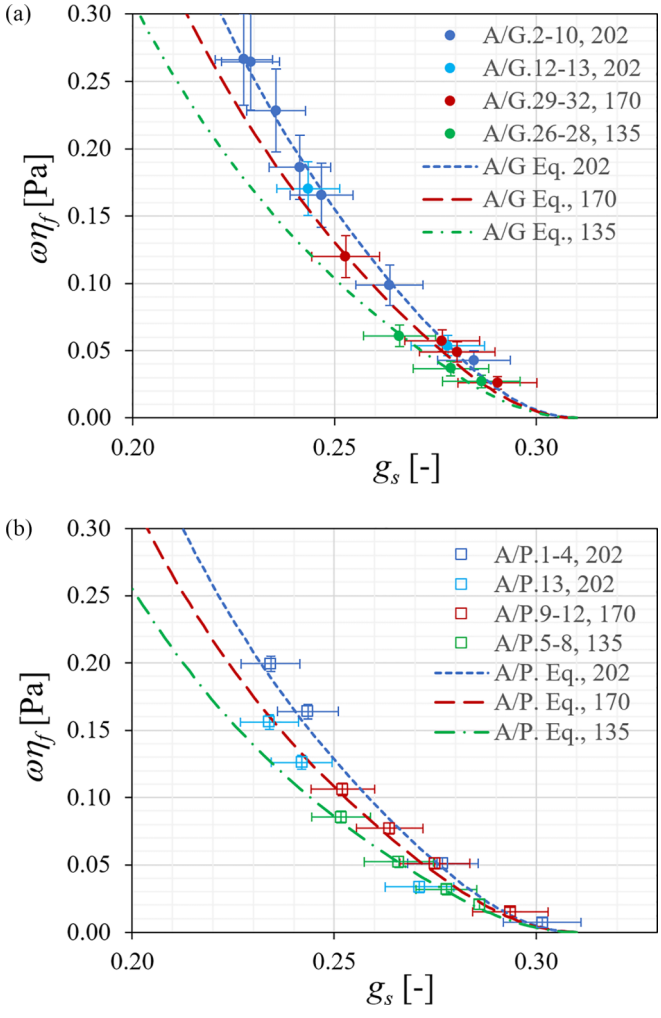

FIG. 7. Rotation speed multiplied by the viscosity of the liquid as a function of solid volume fraction for A particles processed in glycerol (a) and in PEG-PPG (b) at different applied torques ($M = 135$, 150, 170, 202 mNm, as also indicated by the numbers given in the legend). The dotted lines were estimated by applying Eq. (7) with $\alpha_0 = 1150\,\mathrm{m}^{-3}$ for A in glycerol (a) and $\alpha_0 = 950\,\mathrm{m}^{-3}$ for A in PEG-PPG (b). The friction coefficient parameters were taken from Table I, with μ_2 and l_0 as given by the Eq. μ_2/I_0 data.

smaller values of l_0 tend to flatten the $\mu - g_s$ curve, while larger values of μ_2 and slightly larger values of l_0 increase the curvature, with the resulting $\mu - g_s$ curves still lying within the range of the error bars. This is illustrated in Fig. 5 by the three curves corresponding to different pairs of μ_2 and l_0 as specified in Table I.

The measured quantities were assumed to be accurate within the following limits: initial solid fraction ± 0.008, force ± 0.15 N, cover position difference ± 0.05 mm, rotation speed $\pm 0.1\,\mathrm{min}^{-1}$, and suspension temperature ± 0.2 K. The applied torque was assumed to be exact. The error bars shown in Figs. 5–8 were calculated using standard error propagation laws.

The friction coefficient was used to calculate the particle pressure as

$$P^p(g_s) = \frac{\alpha_M M}{\mu(g_s)}, \tag{6}$$

where the shear stress τ is linearly related to the torque M via $\tau = \alpha_M M$, with $\alpha_M = 723.19\,\mathrm{m}^{-3}$ for the present experimental setup. The corresponding agreement of the measured particle pressure with Eq. (6) is illustrated in Fig. 6 for A and C particles processed in both glycerol and PEG-PPG. As discussed below, the measured particle pressure has not been corrected for buoyancy effects.

Figures 7 and 8 show measurements of the product of the rotation speed, ω, and the viscosity of the liquid, η_f, as a function of g_s for A and C particles processed in glycerol and in PEG-PPG, respectively. η_f has been taken to be temperature-dependent. These measurements follow the equation

$$\omega\eta_f = \frac{\alpha_0 M}{\mu(g_s)}\left(\frac{g_{s,c} - g_s}{g_s}\right)^2, \tag{7}$$

with $\alpha_0 = 1150\,\mathrm{m}^{-3}$ and $\alpha_0 = 950\,\mathrm{m}^{-3}$ for A particles in glycerol and PEG-PPG, respectively, and $\alpha_0 = 1500\,\mathrm{m}^{-3}$ for

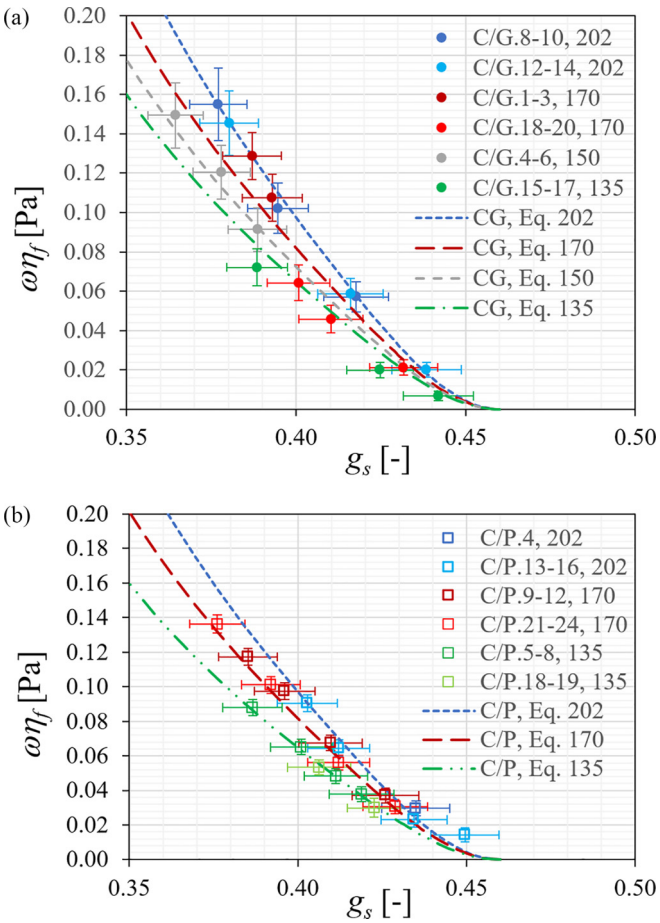

FIG. 8. Rotation speed multiplied by the viscosity of the liquid as a function of solid volume fraction for C particles processed in glycerol (a) and in PEG-PPG (b) at different applied torques (M = 135, 150, 170, 202 mNm, as also indicated by the numbers given in the legend). The dotted lines were estimated by applying Eq. (7) with $\alpha_0 = 1500\,\mathrm{m}^{-3}$ for both cases. The friction coefficient parameters were taken from Table I, with μ_2 and l_0 as given by the Eq. μ_2/I_0 data.

C particles and $\alpha_0 = 1050\,\mathrm{m}^{-3}$ for B particles (results not shown).

IV. DISCUSSION

In contrast to spherical particles, OSP6-like particles—particularly those with longer arms (A-type)—may experience non-negligible Coulomb wall friction. Unfortunately, the existing dataset does not allow even an approximate quantification of this effect. If present, wall friction would affect both the estimated shear stress, τ, and pressure, P^p, to a similar extent, resulting in a uniform upward shift of the $\mu(g_s)$ curve. This limitation is inherent to the present experimental design.

Owing to the different densities, OSP6 particles float in glycerol but sink in PEG-PPG. Consequently, buoyancy is expected to contribute a positive pressure for particles in glycerol and a negative pressure for particles in PEG-PPG. Initially, this effect was taken into account by adding the buoyancy correction $P_{\mathrm{buoy}} = g(\rho_{\mathrm{particle}} - \rho_{\mathrm{liquid}})g_{s,0}V_0/(\pi(R_1^2 - R_2^2))$ to the measured pressure. Depending on the initial particle volume fraction, $g_{s,0}$, used in the initial suspension volume, V_0, this correction ranged from -3.9 to $-5.9\,\mathrm{N/m^2}$ for particles in glycerol and from 3.6 to $5.3\,\mathrm{N/m^2}$ for particles in PEG-PPG. As a result, the $\mu - g_s$ curve for particles in glycerol was consistently shifted above that for PEG-PPG.

However, according to Boyer *et al.* [27], the friction coefficient of a suspension should be independent of the suspending liquid. This is supported by our observations: when no buoyancy correction is applied, the $\mu - g_s$ measurements for particles in glycerol and in PEG-PPG collapse onto a single curve, as shown in Fig. 5.

It is evident that particles that are strongly entrained by a fluid in horizontal motion do not exert a buoyancy force on objects from which they are separated. Consequently, the lower the solid fraction and the higher the rotation rate, the smaller the influence of buoyancy. Conversely, in densely packed suspensions, the particle pressure turns out to be much larger than the buoyancy-related pressure correction evaluated above. In both cases, a buoyancy correction can be neglected.

Consistent with the findings from Olmedilla *et al.* [10], our experimental results confirm that the solid volume fraction at which the viscosity of the suspension diverges, $g_{s,c}$, is lower for particles with low sphericity. This behavior can be attributed to the presence of large sidearms on the particles, which interlock at relatively low solid volume fractions. In the solidification community, it is well established that pressure can be transmitted through a solid skeleton only beyond the mechanical coherency (or rigidity) point, rather than the dendritic coherency point, where crystals first come into contact [23].

In the present experiments, the particle pressure is an intrinsic quantity that arises even in the absence of external forces. Although jamming becomes more pronounced for $g_s \to g_{s,c}$, pressure transmission remains unlikely; only for $g_s \geqslant g_{s,c}$ can pressure be transmitted through the closely packed particle ensemble. Therefore, $g_{s,c}$ corresponds to the mechanical coherency point referred to by the solidification community.

The observation that μ_1, the friction coefficient at $g_s \simeq g_{s,c}$, increases with decreasing sphericity is unsurprising, as a larger particle surface area (at equal volume) results in rougher interparticle interfaces. The obtained values for μ_2 and I_0 do not show a clear correlation with sphericity. However, the $\mu - g_s$ curves for dendrite-like particles exhibit a higher curvature than those for spherical particles.

The fact that the values for μ_2 and I_0 estimated in this work are somewhat imprecise raises the question of the accuracy of the values suggested by Boyer *et al.* [27] for spherical particles. Based on our experience, it seems plausible that the μ measurements reported by Boyer *et al.* could also be reasonably approximated by a slightly different set of μ_2 and I_0 values. Unfortunately, the authors did not report uncertainties for $g_{s,c}$, μ_1, μ_2, and l_0.

Assuming that the shear rate is linearly related to the rotation speed, as $\dot{\gamma} = \alpha_\omega \omega$, Eq. (7) can be derived from the definitions of μ, I_v, and Eq. (4) with $\alpha_\omega = \alpha_M/\alpha_0$. Boyer *et al.* [27] assumed linear shearing along the height of the cell and expressed α_ω as the ratio of the mean radius of the rheometer cell to its mean height, yielding values of $\alpha_\omega = \bar{r}/\bar{h} = 4.3 - 5$ depending on the actual cover position.

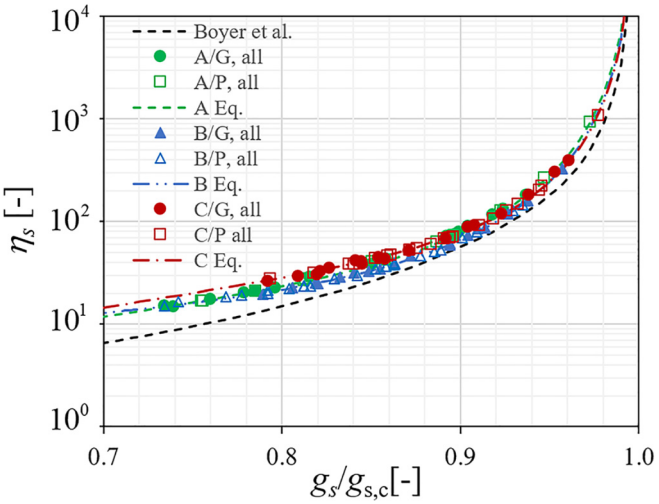

FIG. 9. Dimensionless shear viscosity as a function of the normalized solid fraction for the different OSP6 particles processed in both glycerol and PEG-PPG.

In the present setup, with $\alpha_0 = 1150\,\mathrm{m}^{-3}$ and $\alpha_0 = 950\,\mathrm{m}^{-3}$ for A-type particles processed in glycerol and PEG-PPG, respectively, $\alpha_0 = 1050\,\mathrm{m}^{-3}$ for B-type particles, and $\alpha_0 = 1500\,\mathrm{m}^{-3}$ for C-type particles processed in both liquids, the corresponding values of α_ω are of the order $\alpha_\omega \approx 0.63$ and 0.76 for A particles, and approximately $\alpha_\omega \approx 0.69$ and $\alpha_\omega \approx 0.48$ for B- and C-type particles. Consequently, for the present experiments, the assumption of a linear shearing along the height is not justified. Instead, the shear profile is most likely nonlinear, with a strong gradient near the top of the suspension, close to the rotating cover. This behavior may be attributed to the nonspherical morphology of the particles and the viscosity of the liquid (at least for the A-type particles that reveal a low sphericity). Note that glycerol has a viscosity of $\eta_f = 1.13$ Pa·s, whereas PEG-PPG of $\eta_f = 2.3$ Pa·s, and thus, motion and rotation of the A-type particles are easier in glycerol compared to PEG-PPG. For the B-type particles, a similar behavior was found. For the C-type particles, which do not have significant sidearms, they behave similarly in both liquids.

Another critical aspect influencing the apparent shear rate is the small ratio of cell height to particle size. The cell height varied between 8.6 and 17.56 mm, whereas the tip-to-tip distance of the A-type particles was 2.6 mm and that of the C-type particle was 1.4 mm. Consequently, the ratio of cell height to particle size ranges only from 3.3 to 6.7 for the A-type particles and from 6.1 to 12.5 for the C-type particles. In their pioneering paper, Boyer *et al.* [27] reported ratios ranging from 7.8 (or 14.8) to 16 (or 30), which ensured a smoother, and probably linear, decrease of the shear rate with depth. It must therefore be acknowledged that the present configuration is not sufficient to measure the shear rate directly.

We therefore rely on the assumption that, for the three kinds of dendrite-like particles, Eq. (5) remains valid, and we accordingly estimate the dimensionless shear viscosity based on $\eta_s = \mu/I_v$. The result is presented in Fig. 9. Note that, for $g_s \to g_{s,c}$, the three curves coincide, while for $g_s \to 0$, they converge toward unity. The assumption that Eq. (5) is valid naturally implies that the dimensionless normal viscosity of the suspension, $\eta_n = 1/I_v$, is satisfied.

Surprisingly, the curve for the suspension containing C-type particles lies above those for suspensions containing A- or B-type particles. Intuitively, one would expect that the closer the particle shape is to a sphere, the more closely the viscosity curve would approach Boyer's curve. The C-type particle shape is indeed much closer to spherical than that of the A- or B-type particles.

However, the C-type particles have planar facets that rub against one another as they move past each other. On the contrary, the A- and B- type particles primarily interact through pointwise contacts, as they predominately pass one another by rotation. In addition, the volume fractions processed with C-type particles (0.35–0.45) are significantly higher than those for A-type (0.21–0.30) or B-type particles (0.28–0.38). Consequently, the probability of particle–particle interference is greater for the C-type particles and thus the additional friction arising from sliding along the planar facets becomes significant.

V. CONCLUSIONS

The present investigation demonstrates that the dependence of the friction coefficient on the solid fraction in dense suspensions containing dendrite-like OSP6 particles follows the same law proposed by Boyer *et al.* [27] for spherical particles. However, the solid fraction at which the suspension viscosity diverges must be adjusted downward to account for the reduced sphericity of the OSP6 particles. Furthermore, the friction coefficient at the jamming point increases as the sphericity decreases. By adopting an appropriate friction coefficient for the different OSP6 particles, both the particle pressure and its dependence on shear stress can be accurately described.

Owing to the shape and larger dimensions at equal volume of the dendrite-like OSP6 particles, the rheometer cell proved to be too shallow to permit direct measurements of the shear rate. Nevertheless, it could be shown that for OSP6 particles the rotation rate still follows the theoretical considerations proposed for spherical particles, as long as the appropriate friction coefficient and jamming limits are considered.

Without knowing the shear rate, it is not possible to evaluate the suspension viscosity directly. However, if the dimensionless viscous number is assumed to be related to the solid fraction in the same manner as proposed by Boyer *et al.* [27] for spherical particles, the suspension shear rate can be estimated and consequently the viscosity of the OSP6 suspensions. This indirect estimation indicates that dense suspensions containing OSP6 particles generally exhibit higher viscosities than those composed of spherical particles. This is understandable, as dendrite-like particles with sidearms have a much greater tendency to jam even at lower volume fractions. During processing, these particles predominantly move past one another by rotation, whereas spheres interact by sliding (and rotating).

Interestingly, OSP6 particles without pronounced sidearms, which more closely resemble spheres, exhibit a higher suspension viscosity than those with long sidearms. This behavior can be attributed to the presence of planar

facets, which may increase friction as the particles slide along these facets. When pronounced sidearms are present, rotation is the predominant mechanism by which particles move past one another, and sliding plays a less significant role.

ACKNOWLEDGMENTS

We are very grateful to Prof. C. Holzer and Dr. I. Duretek from the Institute of Polymer Processing at the Technical University Leoben for providing access to the rheometer and for their valuable support. We also thank the company LayerLab, Graz, for producing the 3D-printed particles with great precision and care. Furthermore, we gratefully acknowledge financial support from the Austrian Science Fund (FWF) under Grant DOI 10.55776/P34993.

DATA AVAILABILITY

The data that support the findings of this article are openly available [28].

[1] W. Kurz and D. J. Fisher, *Fundamentals of Solidification*, 4th ed. (Trans. Tech. Publ., Aedermansdorf, 1998).
[2] J. A. Dantzig and M. Rappaz, *Solidification*, 2nd ed. (EPFL Press, Lausanne, 2016).
[3] M. Torabi Rad, M. Založnik, H. Combeau, and C. Beckermann, Upscaling mesoscopic simulation results to develop constitutive relations for macroscopic modeling of equiaxed dendritic solidification, Materialia **5**, 100231 (2019).
[4] G. Zimmermann, L. Sturz, Y. Z. Li, C. Gandin, R. Fleurisson, C. Beckermann, and A. Karma, Columnar and equiaxed solidification of Al-7 wt.% Si alloys in reduced gravity in the framework of the CETSOL project, JOM online **69**, 1269 (2017).
[5] K. Fezi, A. Plotkowski, and M. J. Krane, Macrosegregation modeling during direct-chill casting of aluminum alloy 7050, Num. Heat Transf. A **70**, 939 (2016).
[6] H. C. de Groh III, P. D. Weidman, R. Zakhem, S. Ahuja, and C. Beckermann, Calculation of dendrite settling velocities using a porous envelope, Met. Trans. B **24**, 749 (1993).
[7] S. Gerardin, H. Combeau, and G. Lesoult, Étude de l'effet du mouvement relatif cristal/liquide sur la croissance d'un cristal dendritique dans un liquide en surfusion, J. Phys. IV **11**, Pr6-143 (2001).
[8] A. Badillo, D. Ceynar, and C. Beckermann, Growth of equiaxed dendritic crystals settling in an undercooled melt, Part 1: Tip kinetics, J. Cryst. Growth **309**, 197 (2007).
[9] A. Badillo, D. Ceynar, and C. Beckermann, Growth of equiaxed dendritic crystals settling in an undercooled melt, Part 2: Internal solid fraction, J. Cryst. Growth **309**, 216 (2007).
[10] A. Olmedilla, M. Založnik, B. Rouat, and H. Combeau, Packing of sedimenting spherical and equiaxed non-convex particles, Phys. Rev. E **97**, 012910 (2018).
[11] J. Ni and C. Beckermann, A volume-averaged two-phase model for transport phenomena during solidification, Met. Trans. B **22**, 349 (1991).
[12] C. Beckermann and R. Viskanta, Mathematical modeling of transport phenomena during alloy solidification, Appl. Mech. Rev. **46**, 1 (1993).
[13] I. M. Krieger and T. J. Dougherty, A mechanism for non-newtonian flow in suspensions of rigid spheres, Trans. Soc. Rheol. **3**, 137 (1959).
[14] I. M. Krieger, Rheology of monodisperse latices, Adv. Colloid Interface Sci. **3**, 111 (1972).
[15] A. Ludwig and M. Wu, Modeling of globular equiaxed solidification with a two-phase approach, Met. Mater. Trans. A **33**, 3673 (2002).
[16] M. Wu, A. Ludwig, A. Bührig-Polaczek, M. Fehlbier, and P. R. Sahm, Influence of convection and grain movement on globular equiaxed solidification, Int. J. Heat Mass Transf. **46**, 2819 (2003).
[17] T. Wang, M. Wu, A. Ludwig, M. Abondano, B. Pustal, and A. Bührig-Polaczek, Modelling the thermosolutal convection, shrinkage flow and grain movement of globular equiaxed solidification using a three phase model, Int. J. Cast Met. Res. **18**, 221 (2005).
[18] C. Y. Wang and C. Beckermann, Equiaxed dendritic solidification with convection Part I: Multiscale/multiphase modeling, Met. Mater. Trans. A **27**, 2754 (1996).
[19] C. Y. Wang and C. Beckermann, Part II: Numerical simulations for an AI-4 Wt Pct Cu alloy, Met. Mater. Trans. A **27**, 2765 (1996).
[20] M. Wu and A. Ludwig, Modeling equiaxed solidification with melt convection and grain sedimentation—I: Model description, Acta Mater. **57**, 5621 (2009).
[21] M. Wu and A. Ludwig, Modeling equiaxed solidification with melt convection and grain sedimentation—II. Model verification, Acta Mater. **57**, 5632 (2009).
[22] A. K. Dahle and D. H. StJohn, Rheological behaviour of the mushy zone and its effect on the formation of casting defects during solidification, Acta Mater. **47**, 31 (1998).
[23] I. Farup and A. Mo, Two-phase modeling of Mushy zone parameters associated with hot tearing, Met. Mater. Trans. A **31**, 1461 (2000).
[24] A. K. Dahle and L. Arnberg, Development of strength in solidifying aluminium alloys, Acta Mater. **45**, 547 (1997).
[25] M. Wu, A. Fjeld, and A. Ludwig, Modelling mixed columnar-equiaxed solidification with melt convection and grain sedimentation–Part I: Model description, Comp. Mater. Sci. **50**, 32 (2010).
[26] T. Haxhimali, A. Karma, F. Gonzales, and M. Rappaz, Orientation selection in dendritic evolution, Nat. Mater. **5**, 660 (2006).
[27] F. Boyer, E. Guazzelli, and O. Pouliquen, Unifying suspension and granular rheology, Phys. Rev. Lett. **107**, 188301 (2011).
[28] DOI: 10.34901/mul.pub.2026.036.
[29] A. Einstein, Eine neue bestimmung der moleküldimensionen, Ann. Phys. **324**, 289 (1906).
[30] A. Einstein, Berichtigung zu meiner arbeit: eine neue bestimmung der moleküldimensionen, Ann. Phys. **339**, 591 (1911).
[31] É. Guazzelli and O. Pouliquen, Rheology of dense granular suspensions, J. Fluid Mech. **852**, 1 (2018).